Materials Advances

PAPER

View Article Online
View Journal | View Issue

Check for updates

Cite this: *Mater. Adv.*, 2022, **3**, 1272

Sublimation of MXene/camphor device: a study on self – destructive dry transiency†

Naveen Bokka, Vivek Adepu and Parikshit Sahatiya *

Recently, transient electronics have come into the limelight on account of their programmable destruction for various exciting biomedical and secure hardware electronics applications, which are impossible to achieve with conventional electronics. Most of the degradation or the destruction process of transient electronic devices relies on wet chemistry, *i.e.*, their dissolution in aqueous and non-aqueous solutions. The triggering of the wet chemistry depends on the availability of the solutions, which is a severe limitation for devices that need to be operated where water/solution availability is scarce. These limitations motivate the exploration a new type of transience materials, where they naturally degrade into the environment without the need for wet chemistry. For the first time, this work demonstrates the fabrication of MXene ($Ti_3C_2T_x$) on a camphor-based device where the camphor (sublimable material) acts as a supporting substrate. The fabricated MXene/camphor device under ambient conditions results in the mechanical fragmentation of the supporting substrate and causes the disintegration of the active material, which leads to the degradation of the device within 15 days. The fabricated device was utilized as a human proximity sensor and as a proof of concept deployed on a tree to demonstrate the disintegration of devices in 15 days. The sensor may find potential applications in defence and strategic missions, among others.

Received 22nd September 2021,
Accepted 6th December 2021

DOI: 10.1039/d1ma00873k

rsc.li/materials-advances

Introduction

The field of transient electronics has emerged with the goal of discarding or destroying the device after its operation.[1–3] Since the inception of this exciting technology, most studies on transient electronics have relied on the degradation of the device using aqueous and nonaqueous solutions.[4–10] These biodegradable electronic devices can be programmed to disintegrate or dissolve in various biofluids, which is impossible to achieve using conventional electronics.[11–13] To overcome this, a non-contact mode of triggering has been utilized to destroy the devices, including humidity and moisture triggering.[14–16] For such triggering to be controlled, there is a dependency on solutions. However, there might be situations wherein the devices developed need to be deployed in places with limited water/solution availability.[17] Furthermore, the toxicity of the water/solution after the destruction of such devices still remains unstudied, meaning that it might still be of concern in terms of water pollution, causing further health hazards. One of the possible solutions to the above issue is to use materials that can degrade over time by themselves without the need for any aqueous and non-aqueous solutions.

In particular, most of the functional nanomaterials being incompatible with transient technology, that restricts the performance of the fabricated devices.[4,18] Most of the materials utilized for transient electronics are biomaterials that do not possess excellent electronic properties. It is a well-known fact that 2D materials are an ideal choice for developing next-generation sensors.[19,20] MXenes are transition metal carbides or nitrides and represent the fastest growing materials among other 2D materials in recent years.[21] Their excellent thermal stability, wide interlayer spacing, hydrophilic nature, and easily tunable structure make them valuable 2D materials, which are not observed for other inorganic 2D materials.[21] MXenes strongly respond to external stimuli, making them very suitable for various sensing applications.[22] The outstanding properties of MXenes including their versatile surface chemistry, excellent electroconductivity, high aspect ratio, and environmentally-friendly nature make them an attractive choice for various applications, ranging from optoelectronics, biomedical, energy storage, gas, and humidity sensing applications.[22,23] Also, functional groups (oxygen, chlorine, hydroxyl, and fluorine) on the surface of MXenes have an impact on their performance in sensing applications.[24] It would thus be fascinating to couple MXenes with transient technology to develop next-generation smart and sustainable electronic devices and sensors.

Department of Electrical and Electronics Engineering, Birla Institute of Technology and Science Pilani Hyderabad Campus, Hyderabad, 500078, India.
E-mail: parikshit@hyderabad.bits-pilani.ac.in

† Electronic supplementary information (ESI) available. See DOI: 10.1039/d1ma00873k

This work demonstrates the development of a proximity sensor that environmentally degrades based on a sublimable material (camphor) as a supporting substrate and an emerging 2D MXene ($Ti_3C_2T_x$) as a functional material and demonstrates its real time application in human tracking. The fabrication process includes the preparation of camphor pellets using a manual pressure gauge (hydraulic press) followed by the drop casting of $Ti_3C_2T_x$ solution. The device undergoes timed self-degradation of the sublimation of the supporting substrate, *i.e.*, camphor breaks down and is released in the air due to chemical reaction with the ambient atmosphere. Camphor sublimation leads to the disintegration of the entire system, resulting in non-functioning of the device due to a lack of mechanical support from the supporting substrate. The reasons for choosing the camphor are due to its low cost, environmentally-friendly nature, and vapor pressure (0.65 mm Hg) at room temperature (25 °C). Finally, as a proof of concept, the fabricated device was attached to a tree to demonstrate its transiency in the natural environment and the device was observed to be completely degraded within 15 days. The device was successfully able to sense human proximity for 5 days and then started to degrade, and after 14 days there was no trace of the device whatsoever. Such systems may find potential applications in defence, security and strategic missions, among others.

The capabilities of such dry transience complement those of commonly studied wet transience. Compared to wet transience, dry transience has advantages because it eliminates the need for aqueous and nonaqueous reactant sources, whose accessibility may be constrained by the natural environment. Similarly, it avoids the use of uncontrolled flows of dissolving liquids that lead to variation in dissolution/reaction rates.

Materials and characterization

MAX (Ti_3AlC_2) powder was procured from Intelligent materials Pvt. Ltd. Hydrochloric acid (HCl, 36–38%) and lithium fluoride (LiF, SRL, 98.5%) were used as obtained without any additional refinement. Commercially available camphor was purchased from local retail stores. MXene/camphor morphology was analyzed using field-emission scanning electron microscopy (FESEM, FEI Apreo Lovac). The electrical characteristics of the fabricated MXene/camphor device were measured using a Keithley 2450 source meter. X-Ray diffraction (XRD) patterns of the prepared MXene and MXene/camphor were obtained using an X-ray diffractometer (Rigaku, Ultima-IV, X-ray source CuKα). The chemical composition of the active material was analysed using a Thermo Scientific K-alpha X-ray photoelectron spectroscopy (XPS) system. A Jasco Fourier-transform infrared (FTIR) spectrometer was employed to analyse the transmission spectra of the prepared MXene/camphor device.

Synthesis of $Ti_3C_2T_x$

The minimally intensive layer delamination (MILD) method was used to etch Al from Ti_3AlC_2. Initially, 0.8 g of LiF was mixed in 10 mL of a HCl (6 M) solution and stirred continuously for 5 min. Then, 0.5 g of Ti_3AlC_2 was added to the above

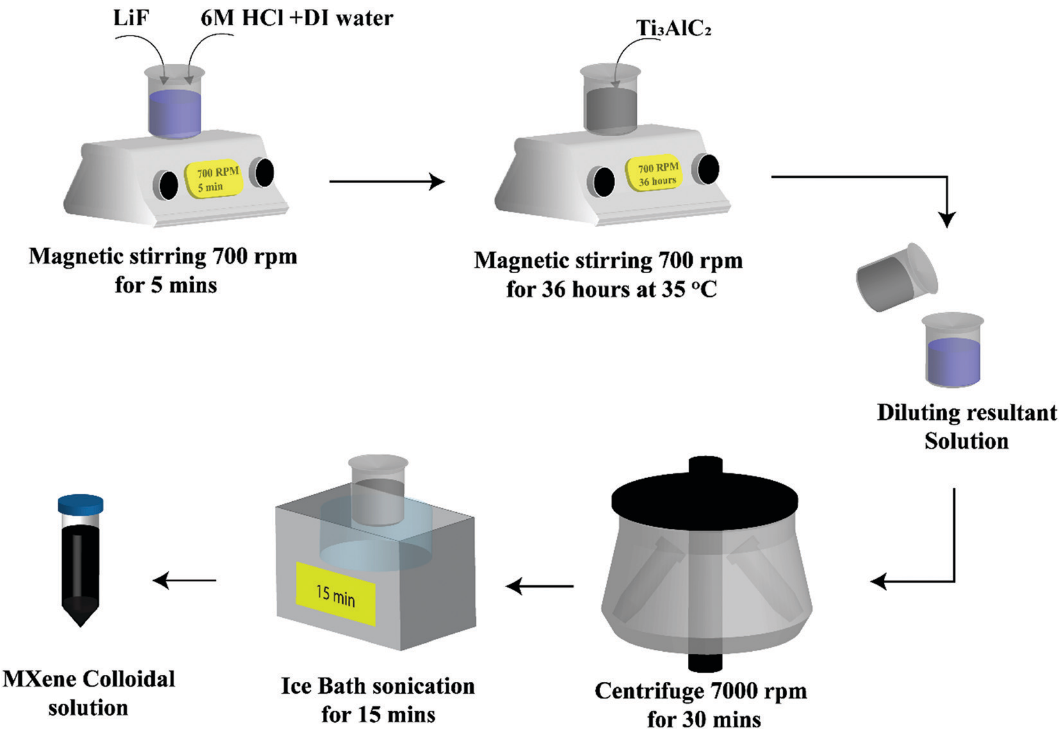

Fig. 1 Schematic of the synthesis of the MXene *via* the MILD method.

prepared solution, which was vigorously stirred for 36 h at 35 °C. Later, the resultant solution was cleaned with deionized water multiple times by centrifugal filtration at 7000 rpm for up to 30 min for each cycle to achieve a solution pH value of ≥6–7. Furthermore, the prepared solution was subjected to ice bath sonication for 1 h. Finally, the resultant $Ti_3C_2T_x$ colloidal solution was kept in the dark to prevent its oxidation.[25] The complete MXene synthesis procedure is shown in Fig. 1.

Fabrication of the MXene/camphor device

The MXene/camphor device fabrication is outlined below. Initially, the camphor pellets were prepared with the help of a manual pressure gauge (hydraulic press). Although camphor pellets are commercially available in general retail stores, the main issue is they are very thick, and also due to the smooth surface of these camphor pellets, the functional material cannot adhere appropriately during the solution casting to the surface of the camphor. To overcome these obstacles, camphor pellets were fabricated with controlled thickness and a rough texture using a hydraulic press. Potassium bromide (KBr) was added to the camphor to form pellets and choosing different ratios is useful for tuning the degradation time of the prepared MXene/camphor devices. During the camphor pellet preparation process, it was noticed that when the KBr concentration was less than 0.5 g in 1 g of camphor, there was less binding, meaning that pellet formation did not happen. Camphor pellets were prepared with different ratios of KBr by maintaining the same concentration of camphor, *i.e.*, 0.5 : 1, 1 : 1, 1.5 : 1 ratios were used for the preparation of camphor pellets. The average force applied to prepare the pellets was 30 ± 2.5 kN. The prepared pellets were carefully placed in a closed environment to avoid evaporation to the surroundings. The prepared pellets were functionalized by $Ti_3C_2T_x$ using a simple drop casting method. $Ti_3C_2T_x$ solution (50 μL) was taken up and drop cast on each pellet and dried for 2 h in an open environment to adhere the MXene to the camphor. The average thickness of the prepared MXene/camphor device was 1.73 ± 0.2 mm. A schematic diagram showing the preparation of the pellets and their functionalization is shown in Fig. 2.

Results and discussion

Extensive characterization was carried out on the structure and morphology of bare MXene and the MXene/camphor device using SEM. Fig. 3a and b show SEM images, wherein the bare MXene has an obviously layered structure.[25] Similarly, to clarify the MXene/camphor morphology, its FESEM image is shown in Fig. 3c. It is obvious from the image that the MXene/camphor material has a uniform and spherical morphology, with an average particle size distribution in the range of 50–70 nm. The SEM image of MXene/camphor/KBr is shown in Fig. 3d, which shows the homogeneous distribution of the grains of KBr over the entire surface of the MXene and camphor. Fig. 3e shows the XRD patterns of Ti_3AlC_2 and $Ti_3C_2T_x$. Where the diffraction peaks at 9.52°, 19.15°, 34.0°, 38.82°, 39.04°, 41.82° and 48.55° correspond to Ti_3AlC_2 (JCPDS 52-0875).[26] After etching Ti_3AlC_2, the removal of Al layers was confirmed, with a change in the peak position from 9.52° to 6.40°, and similarly, the disappearance of a peak at 39.04°. These XRD results confirm the formation of 2D $Ti_3C_2T_x$.[27] The MXene/camphor/KBr peaks are shown in Fig. 3f, with the MXene and camphor peak observed at around 6–20°, and the remaining peaks at 23.83°, 27.12°, 38.62°, 45.7°, 47.82°, 55.71°, 63.24° belonging to KBr.[28–30] Furthermore, to verify the functional groups of

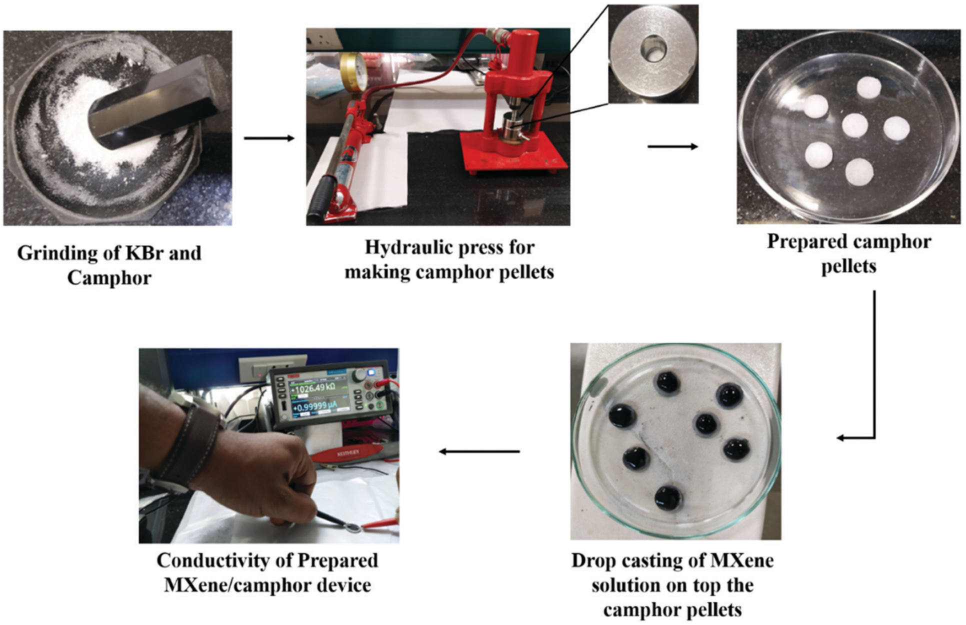

Fig. 2 Fabrication of the MXene/camphor device.

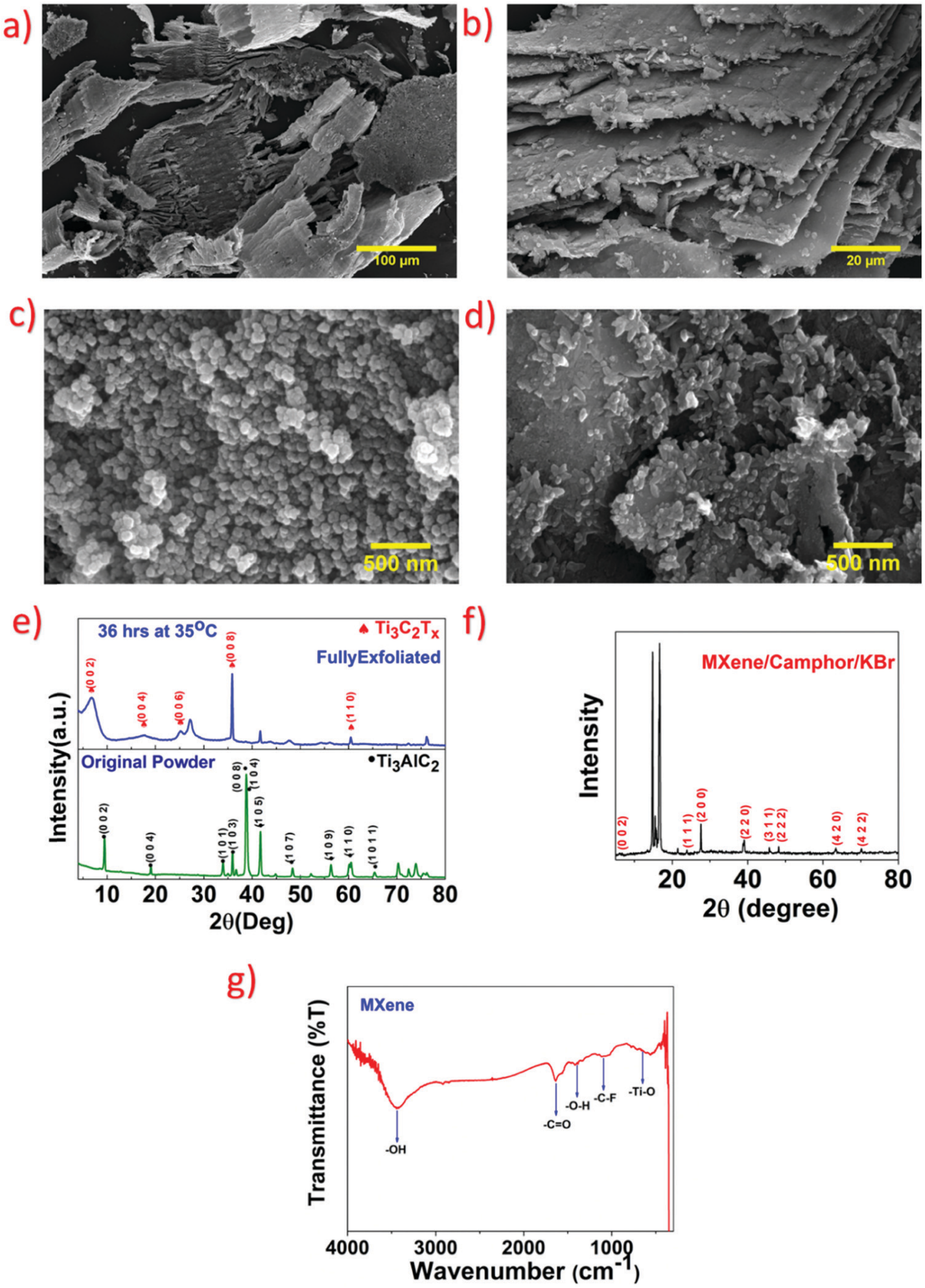

Fig. 3 Characterization of the prepared MXene and MXene/camphor device. (a and b) Morphology of multilayer MXene. (c and d) Morphology of the fabricated MXene/camphor and MXene/camphor KBr. (e) XRD patterns of the original powder (Ti_3AlC_2) and fully exfoliated MXene ($Ti_3C_2T_x$). (f) XRD pattern of the prepared MXene/camphor/KBr device. (g) FTIR spectrum of MXene in the range of 400–4000 cm^{-1}.

MXene, FTIR analysis was performed, with the results shown in Fig. 3g. The stretching vibrations of the Ti–O, C–F, O–H, C=O, and –OH bonds at peak positions of 662, 1100, 1390, 1630, and 3430 cm^{-1} are in good agreement with those given in previous reports.[31,32] Furthermore, the ultraviolet (UV)-visible (UV-vis) spectrum of the pristine MXene, measured utilizing a UV-vis spectrophotometer, is shown in Fig. S1 in the ESI.†

Fig. 4a shows the XPS survey spectrum of pristine $Ti_3C_2T_x$, with binding energies (BEs) in the range of 0–800 eV. The deconvolution of the XPS spectra for the individual elements (*i.e.*, Ti 2p, C 1s, F 1s, and O 1s) was done using the Shirley algorithm. Fig. 4b depicts the high-resolution deconvoluted and fitted spectra for Ti 2p, wherein the pair of $2p_{3/2}$ and $2p_{1/2}$ peaks present at a BE of 454.58 and 461.32 eV can be attributed to Ti–C (sp^3), at 456.88 and 462.55 eV can be ascribed to $Ti^{3+}(sp^1)$ oxide and also at 459.28 and 464.46 eV can be attributed to Ti–O(sp^1) oxide.[33] Also, peaks for $Ti^{2+}(sp^3)$ ($2p_{3/2}$) and Ti–O–F(sp^1) ($2p_{3/2}$) are observed at BEs of 455.55 and

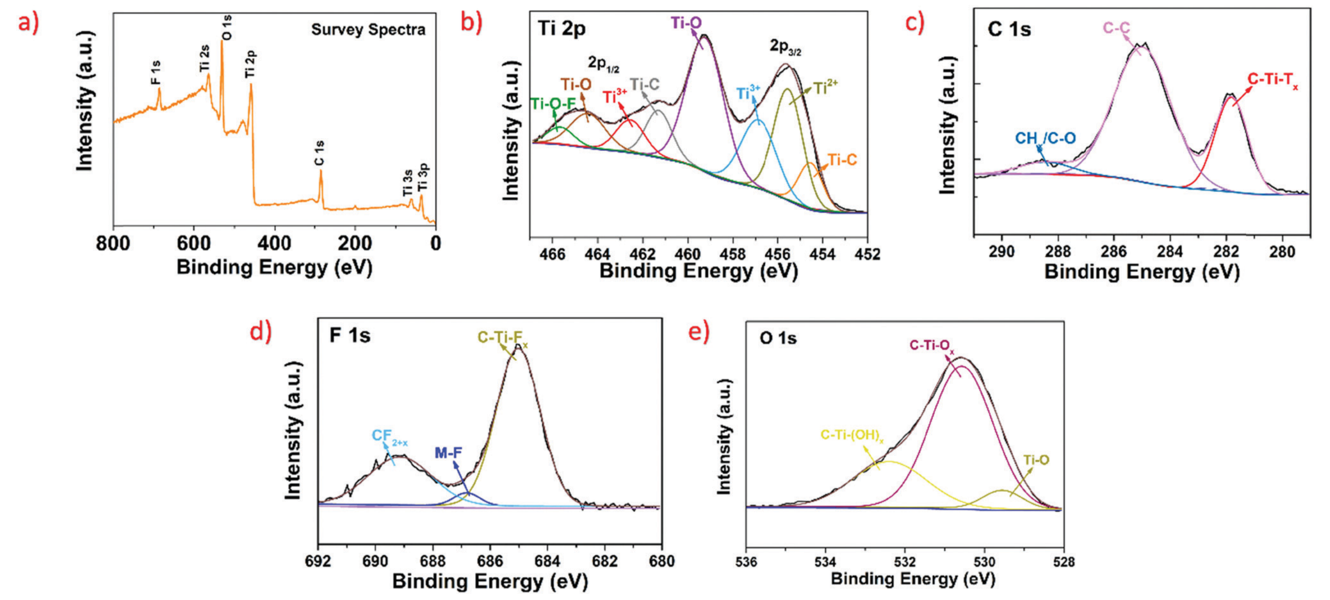

Fig. 4 (a) XPS survey spectrum of the prepared MXene. (b–d) and (e) XPS deconvoluted and fitted spectra of Ti 2p, C 1s, F 1s, and O 1s, respectively.

465.65 eV, respectively.[34,35] The high-resolution deconvoluted XPS spectrum of C 1s is displayed in Fig. 4c, in which the two main peaks ascribed to C–Ti–T_x and graphitic C–C can be observed at BEs of 281.86 and 284.96 eV, respectively, with a new peak at 287.99 eV attributed to CH_x/C–O.[36] Fig. 4d shows the deconvoluted and fitted high-resolution XPS spectra for F 1s, wherein the most prominent peak attained at a BE 685.04 eV can be ascribed to C–Ti–T_x.[37] In addition, the peak at 689.21 eV can be ascribed to CF_{2+x}, owing to the arrangement of polymeric chains with CF_2 of CF_3 groups[38] and the peak at 686.75 eV can be assigned to an anonymous fluorinated subordinate phase or F atoms directly bonded to $Ti_3C_2T_x$ carbon atoms exposed owing to the suspension of some Ti atoms.[39] The high-resolution deconvoluted XPS spectrum for O 1s is shown in Fig. 4e, wherein the contributions ascribed to C–Ti–O_x, C–Ti–$(OH)_x$ and Ti–O were attained at 530.62, 532.65, and 529.70 eV, respectively.[36,40] In particular, minimal oxidation occurred due to the entire synthesis of the nano-layered $Ti_3C_2T_x$ using the MILD method being performed under normal atmospheric conditions.

Degradation mechanism of the MXene/camphor device

The degradation of the MXene/camphor device is as follows. Initially, prepared devices were attached to an acrylic sheet with the help of double-sided tape and placed in an open environment at temperature between 25 and 38 °C. Fig. 5a shows the FTIR transmission spectra and a digital image of the prepared devices (1 : 1) on the first day. Overlapped regions of the fabricated MXene/camphor device are clearly visible in the transmission spectra, where the camphor peaks are dominant in comparison to those of the MXene peaks in account of their methyl stretching (CH_3), methyl bending (CH_3), and ketone (C=O) functional group peaks at 2964, 1445, and 1728 cm^{-1}, shown in red colour.[41] The transmission spectra show that the functional groups CH_3 (stretching), CH_3 (bending), and C=O absorb 97%, 78%, and 99% IR light, respectively. Similarly, 73% was absorbed by the OH functional group of MXene. It is well known that more polar bonds exhibit stronger absorption than less polar bonds. Digital images are shown on the right side of the transmission spectra, of their front and side views, showing the prepared MXene/camphor devices on an acrylic sheet with no degradation. Fig. 5b depicts the transmission spectra of the device after five days, and it was noticed that the prepared device starts degrading owing to a decrease in the absorbance of the camphor functional groups, wherein CH_3 (stretching), CH_3 (bending), and C=O absorb 26%, 15%, and 36%, respectively. The digital images show the sublimation of the MXene/camphor device after five days. A similar trend was observed for the tenth and fifteenth days, as shown in Fig. 5c and d, where the lowest absorbance of the camphor functional groups was 3%, 2%, and 3%, respectively, leaving KBr and MXene residues. In all of the cases, the OH group of MXene absorbance was between 75% and 85%. The sublimation of the device can be ascribed to the solids turning to liquid upon applying heat, with further heating of the liquid to turn it to gas. In contrast, substances or materials can directly become gaseous when heated without turning into liquids, known as sublimation. Camphor is a sublimable material that can be converted into a gas without passing through an intermediate liquid phase. Camphor turns into a gas due to its weak forces between the camphor molecules as even an environmental temperature is enough for camphor molecules to escape to the surrounding environment. The fabricated MXene/camphor under ambient condition slowly loses its mechanical strength, and the disintegration of the active functional material leads the ceasing of the functioning of the device. The sublimation of different ratios of KBr in MXene/camphor devices with respect to degradation time (in days) is shown in Fig. S2 in the ESI.†

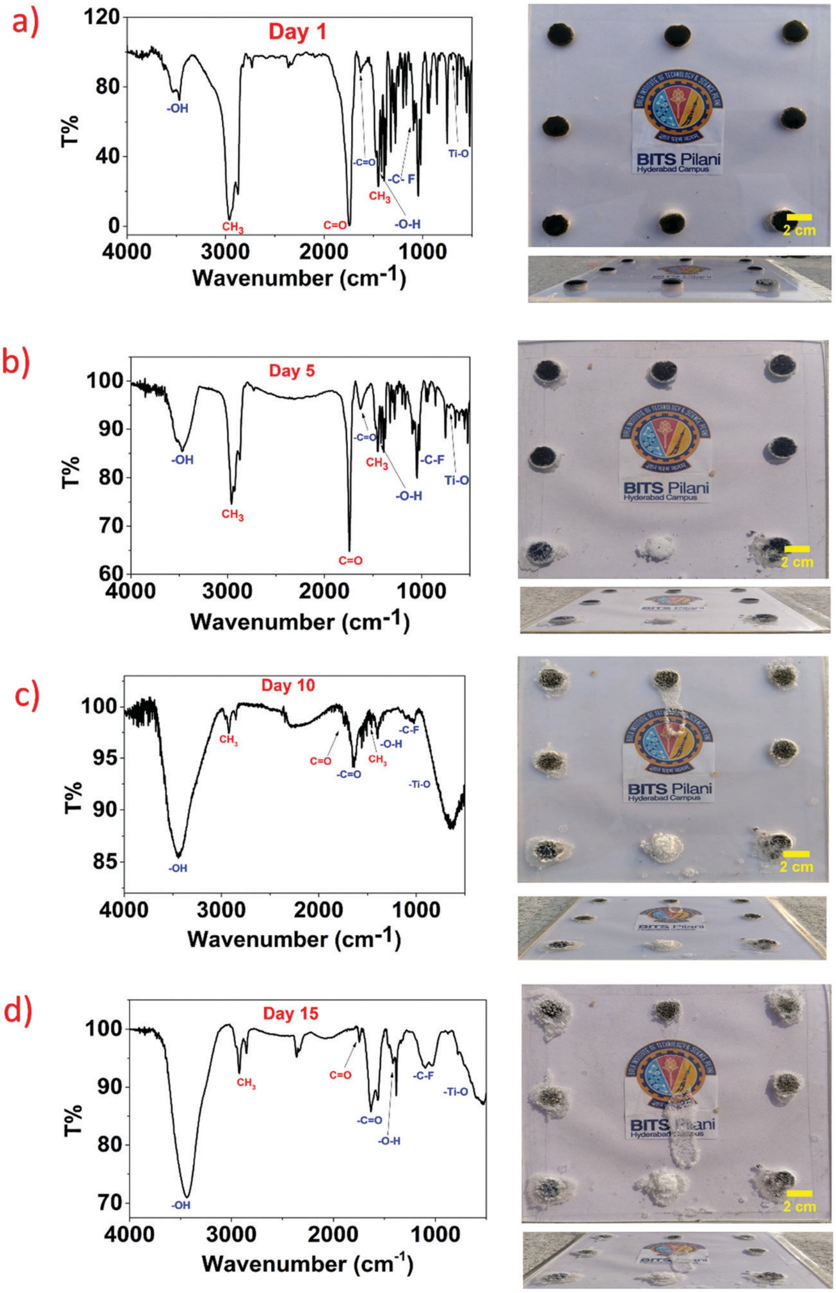

Fig. 5 The degradation mechanism of the fabricated MXene/camphor device. (a) FTIR spectra of the MXene/camphor device on the first day and digital images of the front and side views of the device. (b) FTIR spectra of the degraded device on the fifth day. (c) Degradation of the device on the tenth day. (d) Complete degradation of the MXene/camphor device on the 15th day.

To understand the effect of the environmental conditions on the sublimation rate of camphor, it is essential to predict the behaviour of the camphor under varying temperature and humidity conditions. The rate of sublimation of camphor increases with an increase in temperature due to its low molecular weight (152.23 g mol^{-1}) and high vapour pressure (0.65 mmHg at 25 °C), as previously reported in ref. 42. Furthermore, it is anticipated that the sublimation rate decreases with increasing relative humidity percentage. The temperature and humidity can be adjusted for controlled transiency which can further allow for the destruction of the device at a set time.

The prepared MXene/camphor device shows resistor characteristics, as depicted in Fig. 6a. The device was entirely degraded due to loss of the mechanical strength of camphor, which leads to increased device resistance. The initial resistance of the prepared device was 10.26 kΩ and increased approximately to 320 MΩ after the fifteenth day. As a proof of concept, the fabricated devices (1 : 1) were attached to a tree, as shown in Fig. 6b. It can be seen that the devices were

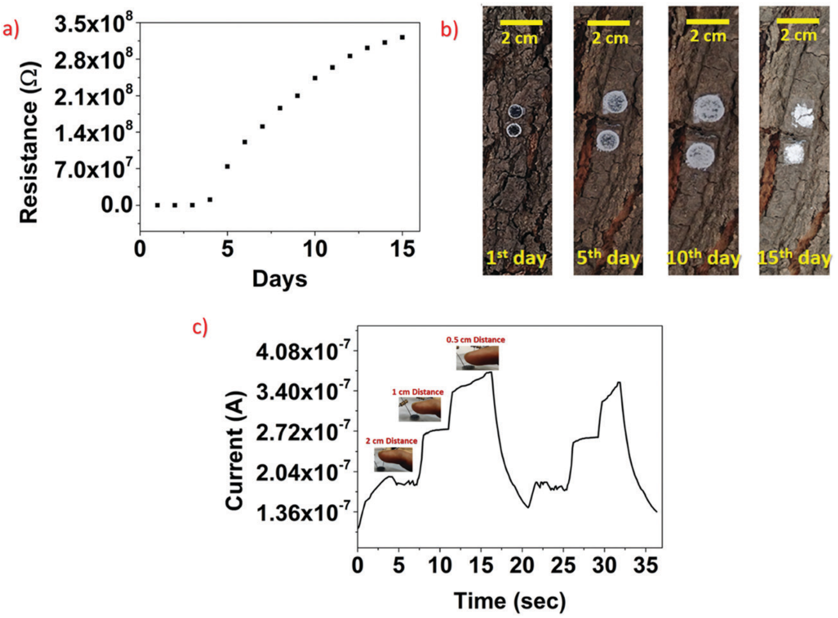

Fig. 6 Application of MXene/camphor devices. (a) Resistance characteristics of the fabricated MXene/camphor device. (b) MXene/camphor devices attached to a tree. (c) Photodetection characteristics of the fabricated MXene/camphor device.

completely disintegrated in 15 days due to sublimation of camphor to the surrounding environment. Fig. 6c shows the photodetection characteristics of the fabricated device when the human body (finger) IR is close to the device. When the finger was at a distance of 0.5 cm, the photocurrent response was increased compared to the distances of 1 and 2 cm. Tests were carried out for the proof of concept of three devices, with the results found to be highly repeatable. The reason for the increase in the device current when bought in close proximity to the human body is that the human body irradiates IR wavelengths. This IR light (although the signal is weak) generates an electron–hole pair in the MXene. Under an external bias of 1 V, the photogenerated electron–hole pairs are separated and are collected at the metal electrode. As the human body is brought closer to the sensor, the intensity of the IR radiation increases and hence more photocurrent was observed. The calculated sensitivity of the proximity sensor with respect to distance and the corresponding photocurrent change was found to be 0.104 μA cm^{-1}. It was confirmed that a fabricated device could identify human body IR radiation, which has tremendous implications in IR imaging and human motion monitoring applications, among others. Responses were obtained by applying an external bias voltage of 1 V.

Conclusion

In summary, a non-contact transient device was fabricated with a strong stimuli response utilizing MXene as a functional material on camphor as a supporting substrate. The transiency of the prepared MXene/camphor devices do not rely on wet chemistry and sublimates under dry and ambient conditions, *i.e.*, camphor breaks down and is released into the air due to its chemical reaction under an ambient atmosphere. The sublimation of the MXene/camphor devices was experimentally proven by FTIR spectroscopy, wherein the device was completely disintegrated within 15 days. Finally, the MXene/camphor device was shown to exhibit resistor characteristics, which were then demonstrated for the NIR sensing of human motion detection. Finally, the device was integrated onto a tree to demonstrate its transiency in a natural environment, and, as predicted, the device completely disintegrated in 15 days. The successful device fabrication and its transiency open up new avenues of research in non-contact transient electronics.

Conflicts of interest

The authors declare no conflict of interest.

Acknowledgements

P. S. acknowledges funding from SERB (SRG/2020/000098). P. S. also acknowledges funding from the Birla Institute of Technology and Science Pilani, Hyderabad Campus (BITS – ACRG). The authors thank the Central Analytical Laboratory, BITS Pilani Hyderabad Campus for the assistance in materials characterization.

References

1 M. J. Tan, C. Owh, P. L. Chee, A. K. K. Kyaw, D. Kai and X. J. Loh, *J. Mater. Chem. C*, 2016, **4**, 5531–5558.
2 K. K. Fu, Z. Wang, J. Dai, M. Carter and L. Hu, *Chem. Mater.*, 2016, **28**, 3527–3539.

3 S. K. Kang, L. Yin and C. Bettinger, *MRS Bull.*, 2020, **45**, 87–95.

4 L. Teng, S. Ye, S. Handschuh-Wang, X. Zhou, T. Gan and X. Zhou, *Adv. Funct. Mater.*, 2019, **29**, 1–9.

5 S. H. Jin, S. K. Kang, I. T. Cho, S. Y. Han, H. U. Chung, D. J. Lee, J. Shin, G. W. Baek, T. Il Kim, J. H. Lee and J. A. Rogers, *ACS Appl. Mater. Interfaces*, 2015, **7**, 8268–8274.

6 N. Bokka, V. Selamneni and P. Sahatiya, *Mater. Adv.*, 2020, **1**, 2818–2830.

7 S. D. Namgung, M. K. Song, T. Sung, O. H. Cho, M. Ju, H. Kim, Y. S. Lee, K. T. Nam and J. Y. Kwon, *Adv. Mater. Technol.*, 2020, **5**, 1–8.

8 C. Dagdeviren, S.-W. Hwang, Y. Su, S. Kim, H. Cheng, O. Gur, R. Haney, F. G. Omenetto, Y. Huang and J. A. Rogers, *Small*, 2013, **9**, 3398–3404.

9 H. Park, Y. Kim, D. Kim, S. Lee, F. S. Kim and B. J. Kim, *Adv. Funct. Mater.*, 2021, **2106977**, 1–9.

10 A. Camposeo, F. D'Elia, A. Portone, F. Matino, M. Archimi, S. Conti, G. Fiori, D. Pisignano and L. Persano, *Adv. Sci.*, 2020, **7**, 1–8.

11 L. Yin, H. Cheng, S. Mao, R. Haasch, Y. Liu, X. Xie, S. W. Hwang, H. Jain, S. K. Kang, Y. Su, R. Li, Y. Huang and J. A. Rogers, *Adv. Funct. Mater.*, 2014, **24**, 645–658.

12 Z. Wei, Z. Xue and Q. Guo, *Micromachines*, 2021, **12**, 6.

13 Y. Choi, J. Koo and J. A. Rogers, *MRS Bulletin*, 2020, DOI: 10.1557/mrs.2020.25.

14 N. Bokka, V. Adepu, V. Selamneni and P. Sahatiya, *Mater. Lett.*, 2021, **290**, 129477.

15 M. A. Brenckle, H. Cheng, S. Hwang, H. Tao, M. Paquette, D. L. Kaplan, J. A. Rogers, Y. Huang and F. G. Omenetto, *ACS Appl. Mater. Interfaces*, 2015, **7**, 19870–19875.

16 Y. Gao, Y. Zhang, X. Wang, K. Sim, J. Liu, J. Chen, X. Feng, H. Xu and C. Yu, *Sci. Adv.*, 2017, **3**, 1–9.

17 B. H. Kim, J.-H. Kim, L. Persano, S.-W. Hwang, S. Lee, J. Lee, Y. Yu, Y. Kang, S. M. Won, J. Koo, Y. K. Cho, G. Hur, A. Banks, J.-K. Song, P. Won, Y. M. Song, K.-I. Jang, D. Kang, C. H. Lee, D. Pisignano and J. A. Rogers, *Adv. Funct. Mater.*, 2017, **27**, 1606008.

18 P. Sahatiya, A. Shinde, A. Kadu and S. Badhulika, *Mater. Sci. Semicond. Process.*, 2019, **93**, 324–330.

19 S. S. Varghese, S. H. Varghese, S. Swaminathan, K. K. Singh and V. Mittal, *Electronics*, 2015, **4**, 651–687.

20 C. Hou, M. Zhang and Q. Chi, in *Two-dimensional Materials – Synthesis,* Characterization and Potential Applications, ed. P. K. Nayak, Intechopen, 2016, ch. 11, pp. 247–270.

21 N. K. Chaudhari, H. Jin, B. Kim, D. San Baek, S. H. Joo and K. Lee, *J. Mater. Chem. A*, 2017, **5**, 24564–24579.

22 X. Jiang, A. V. Kuklin, A. Baev, Y. Ge, H. Ågren, H. Zhang and P. N. Prasad, *Phys. Rep.*, 2020, **848**, 1–58.

23 Y. Zhang, L. Wang, N. Zhang and Z. Zhou, *RSC Adv.*, 2018, **8**, 19895–19905.

24 H. Riazi, G. Taghizadeh and M. Soroush, *ACS Omega*, 2021, **6**, 11103–11112.

25 V. Adepu, V. Mattela and P. Sahatiya, *J. Mater. Chem. B*, 2021, **9**, 4523–4534.

26 Z. Yu, W. Feng, W. Lu, B. Li, H. Yao, K. Zeng and J. Ouyang, *J. Mater. Chem. A*, 2019, **7**, 11160–11169.

27 M. Alhabeb, K. Maleski, B. Anasori, P. Lelyukh, L. Clark, S. Sin and Y. Gogotsi, *Chem. Mater.*, 2017, **29**, 7633–7644.

28 Y. Tanaka, K. Hagano, T. Kuno and K. Nagashima, *J. Cryst. Growth*, 2008, **310**, 2668–2672.

29 D. Febriantini, A. H. Cahyana and R. T. Yunarti, *IOP Conf. Ser.: Mater. Sci. Eng.*, 2019, **509**, 012036.

30 J. U. Maheswari, C. Krishnan, S. Kalyanaraman and P. Selvarajan, *Phys. Rev. B: Condens. Matter Mater. Phys.*, 2016, **502**, 32–38.

31 Q. Xue, H. Zhang, M. Zhu, Z. Pei, H. Li, Z. Wang, Y. Huang, Y. Huang, Q. Deng, J. Zhou, S. Du, Q. Huang and C. Zhi, *Adv. Mater.*, 2017, **29**, 1604847.

32 P. Yan, R. Zhang, J. Jia, C. Wu, A. Zhou, J. Xu and X. Zhang, *J. Power Sources*, 2015, **284**, 38–43.

33 O. Mashtalir, M. Naguib, V. N. Mochalin, Y. Dall'Agnese, M. Heon, M. W. Barsoum and Y. Gogotsi, *Nat. Commun.*, 2013, **4**, 1–7.

34 S. Elumalai, M. Yoshimura and M. Ogawa, *Chem. – Asian J.*, 2020, **15**, 1044–1051.

35 J. Zhu, Y. Tang, C. Yang, F. Wang and M. Cao, *J. Electrochem. Soc.*, 2016, **163**, A785.

36 P. A. Rasheed, R. P. Pandey, K. Rasool and K. A. Mahmoud, *Sens. Actuators, B*, 2018, **265**, 652–659.

37 J. Ma, W. Li, B. J. Morgan, J. Światowska, R. Baddour-Hadjean, M. Body, C. Legein, O. J. Borkiewicz, S. Leclerc, H. Groult, F. Lantelme, C. Laberty-Robert and D. Dambournet, *Chem. Mater.*, 2018, **30**, 3078–3089.

38 M. Benchakar, L. Loupias, C. Garnero, T. Bilyk, C. Morais, C. Canaff, N. Guignard, S. Morisset, H. Pazniak, S. Hurand, P. Chartier, J. Pacaud, V. Mauchamp, M. W. Barsoum, A. Habrioux and S. Célérier, *Appl. Surf. Sci.*, 2020, **530**, 147209.

39 T. Sultana, G. L. Georgiev, G. Auner, G. Newaz, H. J. Herfurth and R. Patwa, *Appl. Surf. Sci.*, 2008, **255**, 2569–2573.

40 J. Halim, K. M. Cook, M. Naguib, P. Eklund, Y. Gogotsi, J. Rosen and M. W. Barsoum, *Appl. Surf. Sci.*, 2016, **362**, 406–417.

41 S. K. Vemula and M. Vangala, *Int. Scholarly Res. Not.*, 2014, **2014**, 1–8.

42 T. Phaechamud, S. Tuntarawongsa and P. Charoensuksai, *AAPS PharmSciTech*, 2016, **17**, 1213–1220.